

A Reconfigurable Convolution-in-Pixel CMOS Image Sensor Architecture

Ruibing Song, *Student Member, IEEE*, Kejie Huang, *Senior Member, IEEE*, Zongsheng Wang, *Student Member, IEEE*, and Haibin Shen

Abstract—The separation of the data capture and analysis in modern vision systems has led to a massive amount of data transfer between the end devices and cloud computers, resulting in long latency, slow response, and high power consumption. Efficient hardware architectures are under focused development to enable Artificial Intelligence (AI) at the resource-limited end sensing devices. One of the most promising solutions is to enable Processing-in-Pixel (PIP) scheme. However, the conventional schemes suffer from the low fill-factor issue. This paper proposes a PIP based CMOS sensor architecture, which allows convolution operation before the column readout circuit to significantly improve the image reading speed with much lower power consumption. The simulation results show that the proposed architecture could support the computing efficiency up to 11.65 TOPS/W at the 8-bit weight configuration, which is three times as high as the conventional schemes. The transistors required for each pixel are only 2.5T, significantly improving the fill-factor.

Index Terms—processing-in-pixel, visual perception, convolutional neural network, CMOS image sensor.

I. INTRODUCTION

WITH the rapid development of image sensors and computer vision, the machines now can “see” and “understand” the visual world. Among various artificial neural networks, Convolutional Neural Network (CNN) has become dominant in various computer vision tasks and is attracting interest across a variety of domains, including object detection [1], face recognition [2], video compression [3], motion transfer [4], etc.

Although CNN has significantly improved visual systems’ performance, they consume numerous operations and huge storage space, making it difficult for end devices to complete the computation independently. Therefore, data capture and analysis are separately carried out in modern visual systems by sensing devices and cloud computers, respectively. A tremendous amount of data transfer leads to a long delay, slow response, and high power consumption [5]. Moreover, in many vision applications, the systems have to work continuously for monitoring or anomaly detection, i.e., surveillance cameras. The low information density has seriously wasted communication bandwidth, data storage, and computing resource.

K.Huang and H.Shen are with the College of Information Science & Electronic Engineering, Zhejiang University, 38 Zheda Road, Hangzhou, China, 310027, and also with Zhejiang Lab, Building 10, China Artificial Intelligence Town, 1818 Wenyi West Road, Hangzhou City, Zhejiang Province, China, email: huangkejie@zju.edu.cn; shen_hb@zju.edu.cn

R.Song and Z.Wang are with the College of Information Science & Electronic Engineering, Zhejiang University, 38 Zheda Road, Hangzhou, China, 310027, email: songruibing@zju.edu.cn; wangzongsheng@zju.edu.cn

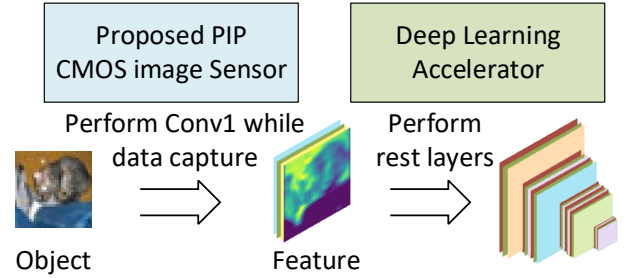


Fig. 1. The first layer of CNN is performed by PIP CMOS image sensor and the rest is done with DLA.

To improve the efficiency of modern vision systems, researchers are focusing on reducing the readout power consumption or data density of sensors [6]–[11]. One of the most promising methods is to enable the computing at the sensing units, which has been intensively studied for with traditional algorithms. For example, [12] computes the difference between the new pixel value and the previous value stored on the in-pixel analog memory to detect motion events, and locates the objects by on-chip computing circuits. [13] adopts a Digital Pixel Sensor Array which has memory, readout circuits, and ADC in each pixel to perform row-parallel motion feature extraction. In-sensor computing with CNN has similar ideas. Computing CMOS Image Sensors (CIS) for CNN can be divided into three categories: (1) Processing-Near-Sensor (PNS), (2) Processing-In-Sensor (PIS), and (3) Processing-in-Pixel (PIP). The PNS architecture utilizes on-chip Deep Learning Accelerators (DLA) to shorten the physical distance between the processor and the image sensor [14]–[16]. The PIS architecture is proposed to reduce the data transfer distance, read operations, and analog-to-digital conversions. For example, Redeye performs several layers of CNN computing in CIS by additional analog arithmetic circuits before readout, saving 85% energy due to the reduced read operations [17]. However, it needs many analog capacitors for data storage, leading to a large area overhead and low computational efficiency. PIP is a fully integrated architecture to enable sensing and computing simultaneously. However, they need complicated pixel circuits, which lead to excessive area and power consumption [18], [19].

The convolution operation of the first layer is usually the performance bottleneck in various acceleration algorithms for the following reasons. The first reason is the limited number

of input channels and parameters in the first layer, leading to the challenge in pruning or quantification. For example, the pruning in [20] and quantification in [21] leave the weight of the first layer unchanged, because it is very sensitive to the accuracy of the network. To support the entire network, DLA must be designed in accordance with the requirements of every layer, leading to the hardware complexity and the computing inefficiency. Furthermore, there are many differences between the structure of the first layer and the subsequent layers, so the computing resources cannot be effectively utilized. The PIP architecture is a possible solution that performs the computing of the first layer while sensing with high efficiency.

Based on the above reasons, we propose a novel PIP architecture as shown in Fig. 1, which moves the operations of the first layer to the sensor to improve the resource utilization and computing efficiency of the DLAs. The proposed PIP architecture can enable highly efficient convolution computation in pixels to improve both fill-factor and computing efficiency. The Multiply-accumulate (MAC) operation is achieved by Pulse Width Modulation (PWM) and pixel splicing. The entire pixel array allows massive parallel convolution operations, generating one complete output feature map in four steps when the stride is two, and the filter size is $3 \times 3 \times 3$. Our proposed architecture could also support 60 frames and 128×128 resolution when the output channel size is 64. Early works such as [12] and [13] only support traditional algorithms and some PIP architectures such as [22] and [23] only support Binary Neural Networks, while our proposed scheme can support various convolution kernels via the proposed “kernel splicing” method. The projected computational efficiency can be as high as 11.65 TOPS/W, which is three times higher than that in the reported literature [14], [22]–[25].

The rest of this paper is organized as follows: Section II presents the related works. Section III introduces the detailed design of our proposed scheme, including the overview architecture, the pixel circuit, the MAC operation, array convolution, and the implementation of other convolution kernel sizes. Section IV analyzes the simulation results. Finally, the conclusion is drawn in Section V.

II. RELATED WORK

Fig. 2 shows the block diagram of different architectures, including traditional architecture, PNS, PIS, and PIP.

Traditional architecture (Fig. 2(a)). As shown in [26], the data capture and data analysis in traditional schemes are usually done in the CIS and server, respectively. As a result, the majority of time and energy is consumed by data transfer. New visual systems should be developed to reduce response time and energy consumption.

PNS architecture (Fig. 2(b)). [27] proposed a stacked, backside-illuminated CIS with a Digital Signal Processor (DSP) dedicated to CNN computation. In [28], the signals are quantized by the ramp Analog to Digital Converters (ADCs) and then computed by the on-chip stochastic-binary convolutional neural network processor. Compared with the traditional architecture shown in Fig. 2(a), PNS architectures reduce the energy consumption of data movement. However,

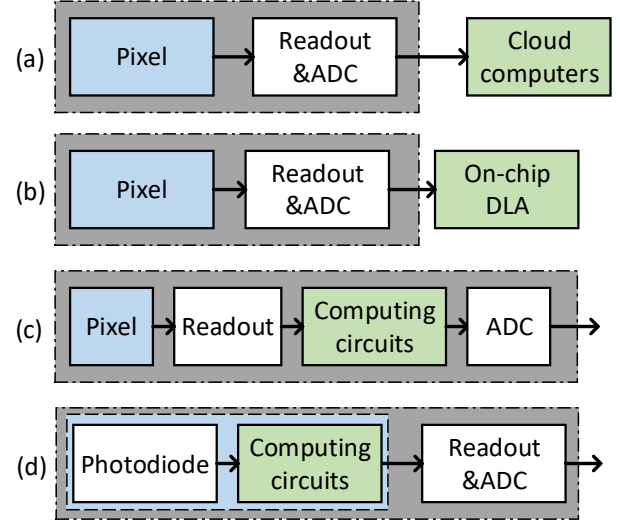


Fig. 2. Different architectures of visual systems. (a)Traditional architecture. (b)PNS architecture. (c)PIS architecture. (d)PIP architecture. Blue boxes represent the pixel, grey boxes mean the sensors, and green boxes show where the computing is conducted.

the energy consumed by the data readout and quantization is still not optimized.

PIS architecture (Fig. 2(c)). In PIS architectures, the computing units are moved to the place before ADC to reduce quantization frequency. Unlike PNS, the computing in PIS is usually done in the analog domain. The CIS in [23] can realize a maximum 5×5 kernel-readout with a minimum of one stride step for convolution operations. Analog processing units directly process the readout signals without ADCs. In [29], input images are captured in the current mode and transferred to the in-sensor analog computing circuit. However, both schemes only support binary neural networks.

PIP architecture (Fig. 2(d)). In PIP architectures, the computing units are integrated with the pixel array. [24] adopted a linear-response PWM pixel to provide a PWM signal for analog-domain convolution. The weights for multiplication are achieved by adjusting the current level and the integral time based on the pixel-signal pulse width. Meanwhile, accumulation is implemented by the current integration. However, the current level is generated by Digital-to-Analog Converter (DACs) according to the weights, which leads to extra power consumption. [18] adopted a pixel processor array-based vision sensor called SCAMP-5. Each pixel contains 13 digital registers and seven analog memory registers to achieve various operations. [22] proposed a dual-mode PIS architecture called MACSen, which has many SRAM cells and computation cells in each unit of the array. Both schemes suffer from a large pixel area and a low fill-factor.

New materials and devices are also developed for PIP architectures to improve the fill-factor. [30] proposed a WSe_2 two-dimensional (2D) material neural network image sensor, which uses a 2D semiconductor photodiode array to store the synaptic weights of the network. However, changing the photosensitivity of the photodiode may need additional DACs

for each pixel to enable massive parallel computing.

Mixed architecture It's usually difficult to conduct all computing tasks with only PIS or PIP architectures. Mixed schemes are thus proposed to achieve the entire neural network computing. In [31], an analog computing circuit is always-on to achieve face detection before ADCs. When faces are detected, the on-chip DLA performs the computing for face recognition in the digital domain, which can be described as a PIS + PNS scheme. [32] fabricated a sensor based on $WSe_2/h - BN/Al_2O_3$ van der Waals heterostructure to emulate the retinal function of simultaneously sensing and processing an image. An in-memory computing unit is added after the sensor to make up the PIP + PNS scheme.

III. PROPOSED ARCHITECTURE

This section describes the detailed design of our proposed PIP architecture, as shown in Fig. 3. The MAC operation is achieved by PWM and pixel splicing, significantly improving the pixel density and computing efficiency. The convolution operations are realized by reconfigurable switching at the array level, allowing massive parallel computing for high performance. The architecture supports the first layer of CNN, which has a low acceleration ratio due to small input channels and large feature maps. It is also very sensitive to pruning [20] and quantization [21]. The proposed CIS can work in the Traditional mode to output the raw image.

A. Pixel Circuit and MAC Operation

As shown in Fig. 3(a), the digital circuit generates the control signals for the pixel array. The detailed designs of the pixel array and pixel circuit are illustrated in Fig. 3(b) and (c), respectively. The convlink wires (shown as green lines) connect adjacent pixel units with splicing transistors in both row and column directions. Each column readout wire (shown as red lines) connects each column of pixel units to a Sample and Hold (S/H) circuit and column ADC, which are the same as traditional CIS. Fig. 3(c) shows the circuit of a pixel unit containing four pixels. Four exposure control transistors $w_1 - w_4$ are connected to a shared FD node. Two reset transistors RST_x and RST_y , a source follower SF , and a row select transistor sel are shared by four adjacent pixels representing RGG channels. Two splicing transistors $conv_out_x$ and $conv_out_y$ control the connection of the convlink wires to the adjacent pixel units in the row direction and column direction, respectively. There are 10 transistors in total for four photodiodes in a pixel unit, and thus each pixel contains 2.5 transistors (2.5T) on average.

Fig. 4 shows the computing flow of the MAC operation with the proposed PIP architecture. The multiplication of photocurrent and weights is realized by controlling the exposure time of photodiodes in each pixel unit. The exposure time of photodiodes is modulated by the weight (8 bit) in the convolution kernel. Pixel splicing method links the FD nodes and averages the multiplication results, thus realizes the accumulation.

Fig. 5 shows the simplified schematic of the proposed pixel in two different modes. Both Traditional and Computing

modes include reset stage, exposure stage, and readout stage. The working mechanism of the Traditional mode is the same as the conventional 1.75T pixel array as shown in Fig.5 (a)-(c) and RST_y is set to low to hand over the reset control to RST_x . The switch between Computing mode and Traditional mode can adopt an event-driven mechanism. When the target object is identified, the CIS can be switched to the Traditional mode to output the complete raw image.

The timing diagram of the Computing mode is shown in Fig. 6, which only contains four pixels for simplicity. A detailed description of each stage in exposure mode is provided as follows:

1) : In the RESET stage, as shown in Fig.5(a), transistors RST_x , RST_y and w_1-w_4 are turned on to reset the potential of the FD node and photodiodes to Vdd. For a Silicon PN photodiode, the rise time is about 5-10 ns [33], which is shorter than our reset time (100 ns). Thus, the photodiode is saturated before the integration begins.

2) : The EXPOSURE stage is started after the RESET stage when RST is de-asserted, as shown in Fig.5(d). In this stage, the control pulses of exposure signals w_1-w_4 are modulated by the weight. The exposure time t_i is proportional to the weight value w_i . Assuming that the convolution kernel size is $r \times r$, one of the MAC operation results can be obtained by connecting r^2 adjacent pixel units with the convlink wires. We assume $r = 3$ as shown in Fig.5(d). The circuit of each pixel unit can be simplified as the FD node connected in parallel with an AC current source. With the convlink wires, the nine FD nodes of the adjacent pixel units and nine AC current sources are connected in parallel. Since the photocurrent I_i is unchanged in a short period, the charge Q stored on each of these FD nodes can be expressed as

$$Q = CU_{rst} - \frac{\sum_{i=1}^{4r^2} (I_i + I_{dc})kw_i}{r^2} \quad (1)$$

where k is the exposure constant, adjusted by the software according to the external light intensity. I_{dc} is the dark current and C is the capacitance of the FD node. Thus, the charge Q on each FD node represents the average of the products of the photocurrent I_i and the corresponding weight value w_i in the convolution kernel. The potential on FD nodes U_{conv} can be expressed as

$$U_{conv} = U_{rst} - \frac{k}{r^2C} \left(\sum_{i=1}^{4r^2} [I_i w_i] - I_{dc} \sum_{i=1}^{4r^2} w_i \right) \quad (2)$$

3) : After the exposure, it is the READOUT stage when sel is asserted, as shown in Fig. 5(e). The weight precision of the convolution kernel used in the system is 8-bit. That is, the weight size of the convolution kernel ranges from -128 to +127. The positive and negative weights of the convolution kernel can be achieved by subtracting two consecutive exposures, as shown in Fig. 6. As w_1 and w_2 are positive, they are enabled in the first exposure period. The negative w_3 and w_4 are enabled in the second exposure period. The digital circuits subtract the two readout operations in Fig. 6 after the ADCs, which is expressed as

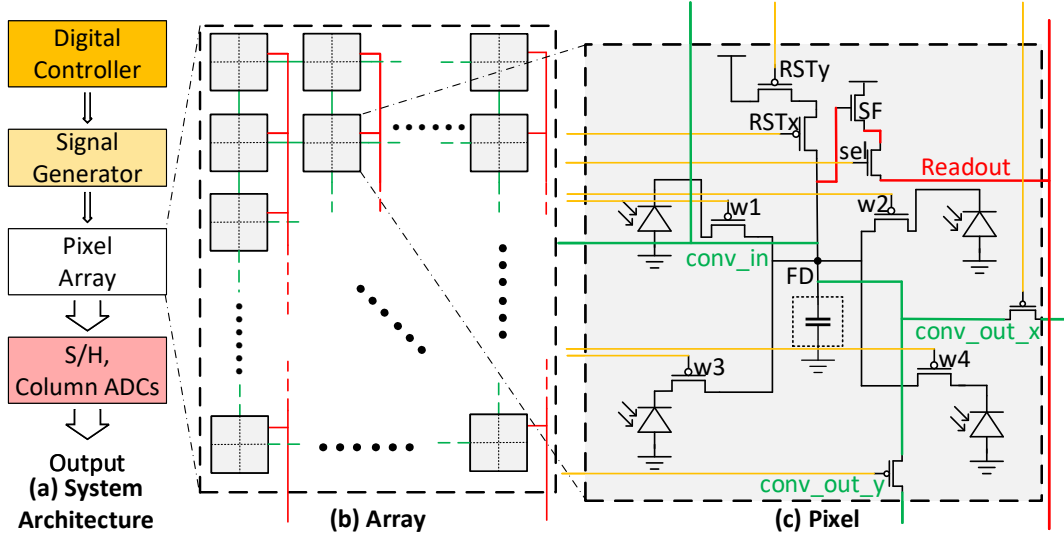


Fig. 3. The overview of the PIP architecture. (a) The system architecture, (b) The structure diagram of the pixel array, and (c) The pixel circuits. The red lines represent the column readout wires, the green lines represent the convlink wires between adjacent pixels, and the golden line shows the direction of the control signals.

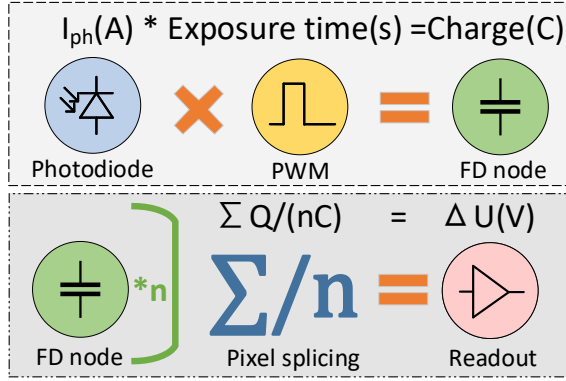


Fig. 4. The computing flow diagram of the proposed architecture.

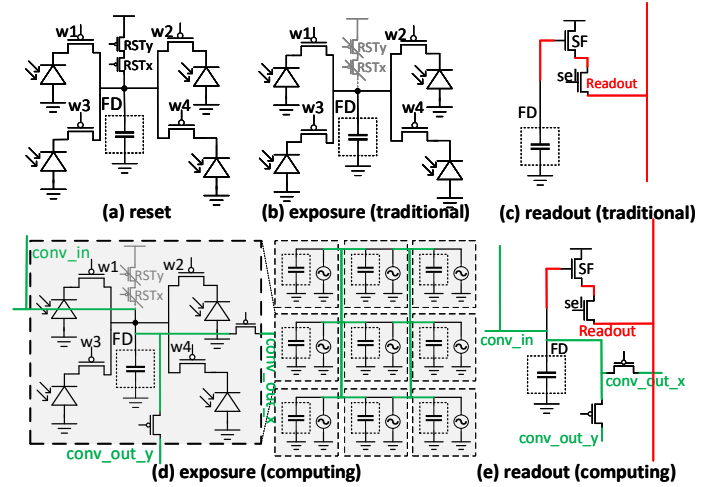


Fig. 5. Proposed pixel circuits in the (a) reset stage, (b) exposure stage in Traditional mode, (c) readout stage in Traditional mode, (d) exposure stage in Computing mode, (e) readout stage in Computing mode. The red lines represent the column readout wires and the green lines represent the convlink wires between adjacent pixels.

$$U = U^- - U^+ = \frac{k}{r^2 C} \left(\sum I_i w_i^+ - \sum I_i |w_i^-| + I_{dc} \sum w_i \right) \quad (3)$$

where $\frac{k}{r^2 C}$ is a known constant, $\sum w_i$ is statistically close to zero and I_{dc} is usually much smaller than I_i . The voltage U_{conv} represents the sum of the r^2 multiplication results, thus achieving MAC operation in-pixel level.

B. Convolution Operation in Array

After introducing the basic idea of the MAC operation, this section gives a detailed introduction to the overall architecture of the system and the sliding convolution on the entire pixel array.

As can be seen from Fig. 3, the most fundamental component of the pixel array is a pixel unit containing four pixels. Splicing transistors separate the adjacent pixel units. Each column of pixel units includes a column S/H circuit and a

column ADC outside the array, which can read the convolution results and convert them into digital signals.

The flow of convolution operation in the array is shown in Fig. 7. In the following example, we assume that the convolution kernel size is 3×3 and the stride is 2. In Fig. 7, each square represents a pixel unit. The 3×3 connected active pixel units are defined as a tile. The horizontal and vertical dash lines mean the break of convlink between the tiles. The entire array can be divided into several independent convolution tiles. The MAC operations are enabled simultaneously in all active tiles in each step. We defined three rows of tiles as a group.

As stated in the previous section, the MAC operation can be achieved by connecting the convlink wires of all pixel units

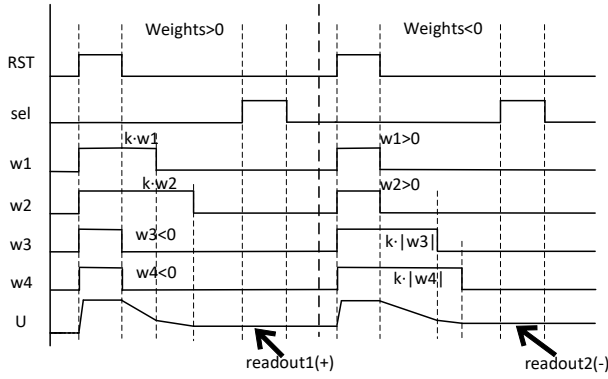


Fig. 6. The convolution sequence diagram of the pixel circuit.

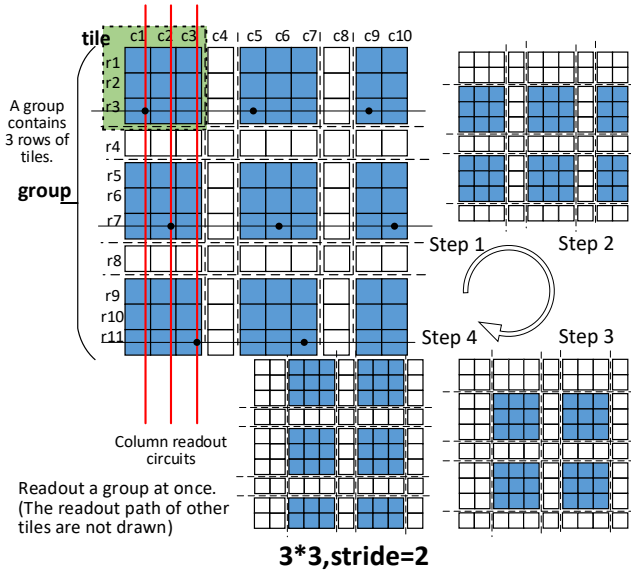


Fig. 7. The flow diagram of the array convolution operation. The convolution kernel size is 3×3 , and the stride is 2. The blue squares represent the active pixels in each convolution step. The green area shows the definition of a tile as an example. The red line represents the column readout circuit.

corresponding to a convolution kernel during computation. More MAC operations should be carried out simultaneously to maximize the parallel operation and computing throughput. Multiple simultaneous MAC operations regions must be non-overlapping, which is achieved by dividing the convolution procedures of the entire array into four steps, as shown in Fig. 7. The colored squares represent the active pixel units, and the uncolored squares represent pixel units not involved in each step. In such a scenario, all the convolution areas can be calculated and read out with only one exposure in one step. The active pixel units perform the MAC operations within the convolution kernel to get a quarter of the convolution result. After four steps of computing, a complete convolution operation is finished. As two exposures are required for the positive and negative weights of each step, eight exposure cycles are needed for each convolution operation.

The above convolution operation needs to plan the hardware wiring carefully. As shown in Fig. 8(a), when the convolution kernel size is 3×3 and stride is 2, pixel units in the same row

are connected to the wire in the following order: $W_1, W_2, W_3, W_2, W_1, W_2, W_3 \dots$. In this way, each tile in a step contains the same wire orders “ W_1, W_2, W_3 ” in the first and second steps and “ W_3, W_2, W_1 ” in the third and fourth steps.

The pixel units in the same column are connected to the same column readout circuit. Each tile includes 3 column readout circuits. To read out the computing results of every three rows of tiles simultaneously, pixel units with the row number x ($x = 4n + 3, n = 0, 1, 2, 3 \dots$) are connected to three independent row enabling signals C_1, C_2, C_3 , as shown in Fig. 8(b). As shown in Fig. 7, the bit lines C_1, C_2 , and C_3 output the computing results of the three consecutive rows of tiles in the vertical direction. In this way, the tiles in one group are read out simultaneously.

The processing sequence of the convolution operation is shown in Fig. 9. The subscript n represents the n^{th} group. As shown in Fig. 9(b), a tile is reset immediately after each readout operation and then begins the exposure for the next readout. Assuming the resolution is 128×128 , the convolution kernel size is 3×3 , the stride is 2, and each step contains 32 rows of convolution kernel results, then each step only needs 11 readout operations. The whole process of array convolution operation is described in Algorithm 1.

This processing sequence has an exception case. The link between pixel units in the same row are realized by splicing transistors controlled in the column direction. As shown in Fig. 10(b), the splicing transistors in the column direction have to be switched when moving from step 2 to step 3 (also when moving from step 4 to step 1). The exposure for step 3 cannot be started until the step 2 has been finished completely. A waiting time should be added between the two steps. For each convolution kernel, this increases the number of equivalent exposure times required from eight to ten. This influence can be ignored when the illumination is strong enough and the ADC frequency becomes the main factor to determine the maximum frame rate.

The readout time of an entire step is $(n_{rd} - 1)T_{rd}$, where T_{rd} is the readout time for each tile and n_{rd} is the number of the readout operations in each step. If the reset interval is T_{rst} , and the maximum exposure time is T_{expo} , the reset and exposure stages need to be finished before the next readout operation,

$$(n_{rd} - 1)T_{rd} > T_{rst} + T_{expo} \quad (4)$$

As shown in Fig. 11, the exposure and readout sequence of the proposed architecture is similar to Interlaced Readout method [34], which divides the readout time for one frame into K sub-images. Compared with the conventional Rolling Shutter as shown in Fig. 11 (a), the Interlaced Readout in Fig. 11 (b) reduces the skew and the time lag in these sub-images K times to support high speed photography, at the cost of the reduction of vertical spatial resolution. Our proposed architecture divides the computing of one frame into 8 groups (each step exposures 2 times for the processing of positive or negative weights) as shown in Fig. 11 (c), which improves the readout speed and resource utilization.

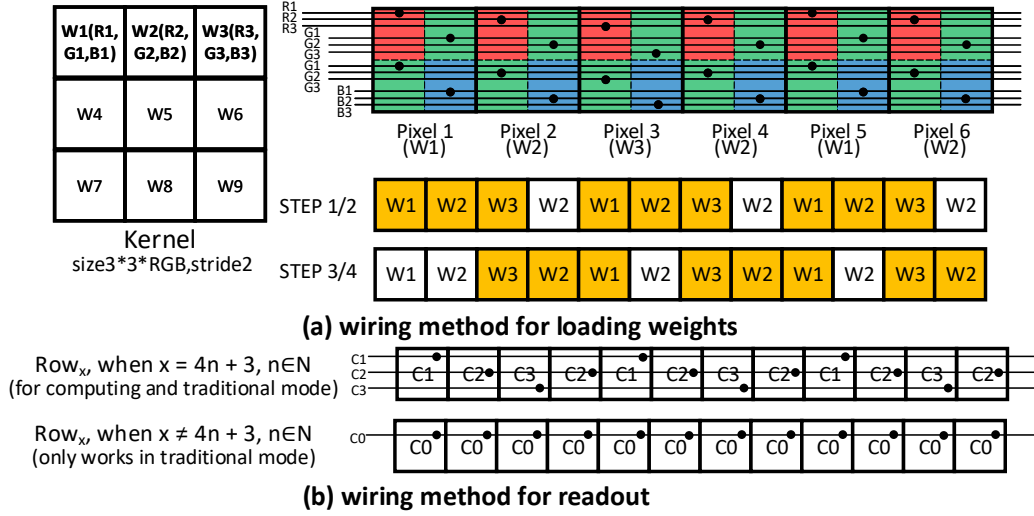


Fig. 8. (a) The wiring way of weight loading. The red, green, and blue squares show the filter RGGGB pattern. The golden squares represent the active pixels in each step. (b) The wiring method for readout. The convolution kernel has a size of 3×3, and the stride is 2.

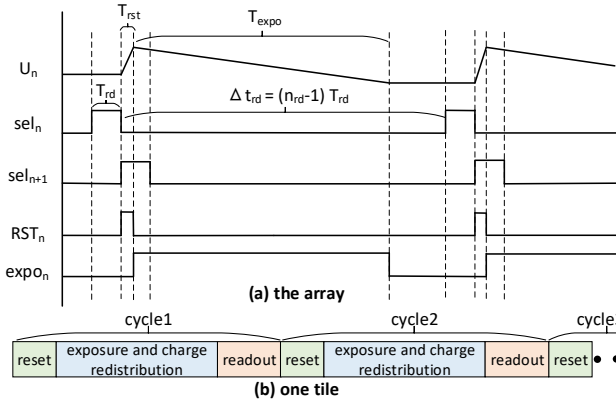


Fig. 9. The convolution operation sequence diagram of (a) the array and (b) one tile. U represents the potential of the FD nodes in the chosen tiles, RST represents the reset stage, $expo$ represents the exposure stage, and rd represents the charge redistribution and readout stage.

C. Implementation of Different Convolution Kernel Size

We propose a “kernel splicing” method to support different kernel sizes with the same wiring method. As shown in Fig. 12(a), 5×5 convolution operation can be realized by two 5×3 convolution operations. The 5×3 convolution operation is similar to the 3×3 convolution operation. The main difference is that the convlink wires link 5×3 pixel units together in the 5×3 convolution operation. The number of steps is changed to 6 instead of 4 because three steps are required in the column direction to avoid overlapping. Each group still has 3 rows of tiles during readout operation. Another two examples for 7×7 and 9×9 kernel sizes are shown in Fig. 12(b) and (c), respectively. In this way, different kernel sizes can be realized by using the same hardware circuits.

Assuming the kernel size is $r \times r$ and the stride is s , the total number of steps is $\frac{r+1}{s}(r-1)$, where the ratio $\frac{r+1}{s}$ needs to round up to an integer if necessary. The equivalent exposure

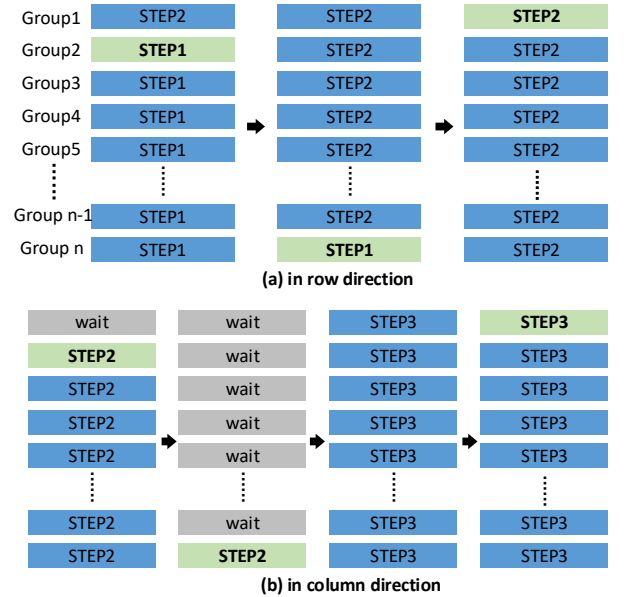


Fig. 10. The different processing sequence between steps when the control signals of splicing transistors are changed (a) in the row direction (such as step 1 to step 2) or (b) in the column direction (such as step 2 to step 3). The blue rectangles represent the groups are in exposure stage, the green rectangles represent the groups are in readout stage, and the grey rectangles mean the groups are waiting for next exposure stage.

times for each channel are $\lceil \frac{2(r+1)}{s} + 1 \rceil (r-1)$. For a fixed height of the pixel array H (128 in our case), the total number of output rows in each step is $\frac{H}{r+1}$. Since each readout operation contains three output rows, the minimum ADC conversion rate can be calculated by

$$f_{ADC(min)} = \frac{2fnH(r-1)}{3s} \quad (5)$$

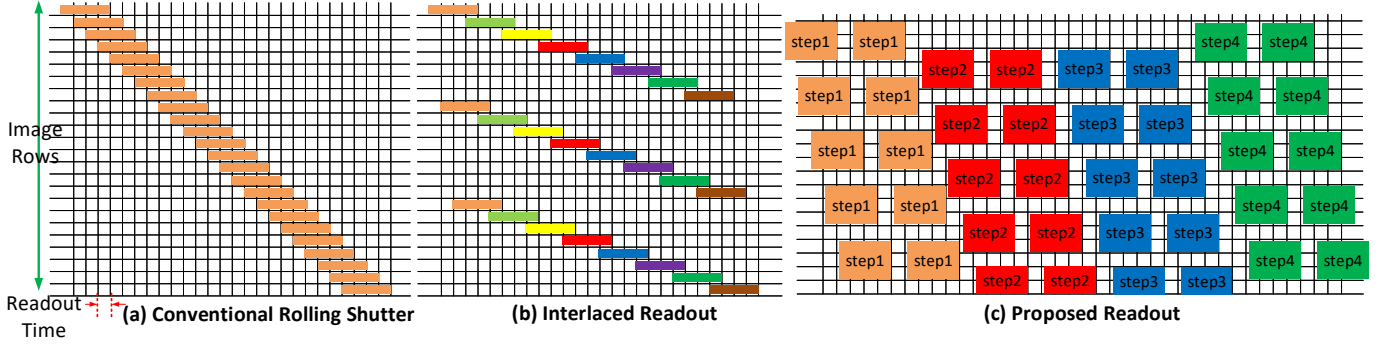


Fig. 11. The exposure and readout sequence diagram of (a) conventional Rolling Shutter, (b) Interlaced Readout, (c) Proposed Readout.

Algorithm 1 Array Convolution Operation

```

1: for each step (1-4) do
2:   Divide the array into independent tiles.
3:   for positive and negative weights(+,-) do
4:     for  $j = 1$  to  $n_{rd}$  (the group serial number) do
5:       Read the results of the three rows of tiles
       via three column readout circuits, respectively.
6:       Reset and exposure group  $j$  for next readout.
       (While continuing to read the next groups
        $j + 1, j + 2 \dots$ )
7:     end for
8:     Calculate the total results by eq. (3).
9:   end for
10: end for

```

where f is the frame rate and n is the number of channels. The minimum conversion rate of ADC is proportional to the frame rate f , the channel number n , and the kernel size r . It is inversely proportional to the stride s .

The actual frame rate f_{real} is defined as the product of frame rate and the output channel number $f \times n$. With a fixed maximum exposure time T_{expo} , the maximum frame rate can be calculated by

$$f_{real(max)} = \frac{s}{[2(r+1)+s](r-1)T_{expo}} \quad (6)$$

The maximum frame rates and the minimum ADC conversion rates at different kernel sizes are tabulated in Table I. For example, the resolution is 128×128 , the stride is 2, the kernel size is 3×3 , the stride is 2, and the output channel number is 64, the maximum exposure time is 26.04 μs . $f_{ADC(min)}$ is based on $f_{real(max)}$ in each condition. When kernel size increases, the conversion rate of ADC will decrease because both actual frame rate and readout operation frequency decrease. As a result, the maximum frame rate decreases.

IV. SIMULATION RESULTS

Our proposed architecture was implemented with TowerJazz 0.18 μm CMOS process. The circuits are simulated with Cadence Virtuoso and Spectre. An analytic model taken from

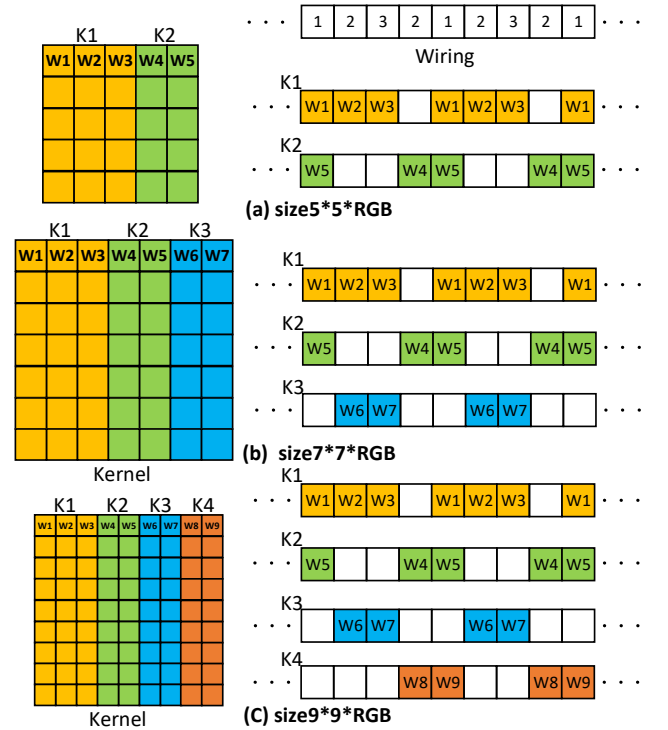


Fig. 12. The convolution implementations of kernel splitting. The convolution kernel size is (a) 5×5 , (b) 7×7 , and (c) 9×9 .

[35] is used to simulate the response of the photodiode. The capacitance of the shared FD node in each pixel units is 22.2 fF, and the responsivity R_λ is about 0.35 A/W at $\lambda = 555$ nm. The photodiode size is set to $10 \mu m \times 10 \mu m$ to collect enough photons. The photocurrent can be estimated as

$$I_{ph} = R_\lambda(P_{in} \times area) \quad (7)$$

where P_{in} represents the input optical power in W/m^2 . The layout design of the pixel is shown in Fig. 13.

The maximum frame rate under different illumination conditions of proposed CIS working in Computing mode and Traditional mode are shown in Fig. 14. In this simulation, the array size is 128×128 , kernel size is 3×3 , the stride is 2, and

TABLE I
RATE CALCULATION WITH DIFFERENT KERNEL SIZES.

operation condition	minimum ADC conversion rate	maximum real frame rate
3×3	327.68 KHz	3840
5×5 (splicing)	234.06 KHz	1371
7×7 (splicing)	182.04 KHz	711
9×9 (splicing)	148.95 KHz	436

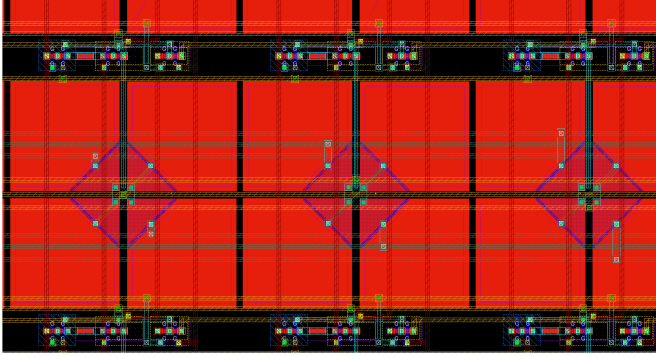


Fig. 13. The layout design of the proposed pixel.

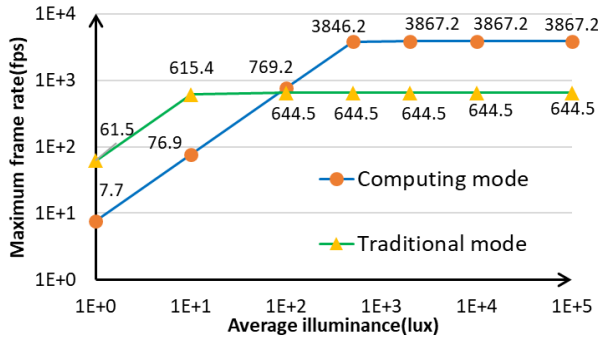


Fig. 14. The maximum frame rate of proposed CIS working in Computing mode and Traditional mode under different illumination conditions.

the ADC conversion rate is 330 KHz. When the light intensity is low, the exposure time is the main factor to determine the maximum frame rate. When the light intensity is high enough, the ADC frequency limits the maximum frame rate. The frame rate of the proposed CIS in Traditional mode is the same as a conventional 1.75T CIS. The proposed Computing mode requires eight times the exposure time of conventional 1.75T CIS for the convolution operation but reduces the readout density. With strong illumination, our proposed CIS in Computing mode outperforms the conventional 1.75T CIS because of the lower readout density.

A. Linearity Simulation

Although FD node behaves electrically as a capacitor, it is quite different from a real capacitor. That is, the non-idealities of the FD node need to be considered in the simulation. Thus,

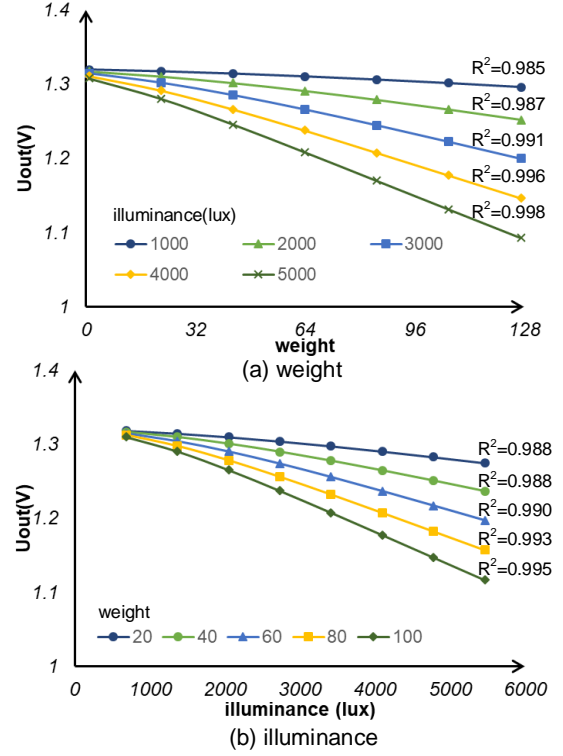


Fig. 15. Simulation of MAC operations. (a) The relationship between readout voltage and weight values at various illuminance. (b) The relationship between readout voltage and illuminance at various weight values.

we use a resistor ($R = 8.07e15 \Omega$, estimated based on the data in [36]) connected in parallel with the FD node to simulate the leakage of the FD node.

Fig. 15 (a) and (b) show the readout voltage U_{out} under different weight and illuminance, respectively. Linear fitting results of both figures show that the R^2 are all above 0.98, indicating high linearity and accuracy of the proposed architecture.

B. Performance Analysis

The power consumption and performance comparison under different conditions are tabulated in Table II. The illumination is about 1500 lux. The array size for all situations is 128×128 , and the number of output channels is 64. The computing results with 5×5 and 7×7 kernels are estimated based on the kernel splicing. The FoM (pJ/pixel/frame) presents the energy consumed per frame (each channel counts once) per pixel. The computing efficiency (TOPS/W) shows the computing amount divided by power consumption. The total computing amount is calculated as the product of the size of the output array, the number of input channels, the number of output channels, the frame rate, and the computing amount for one kernel. When the kernel size is 3×3 , each kernel needs 18 OPs, and the total amount is $64 * 64 * 4 * 64 * 60 * 18 = 1132462080$ OPs. The power consumption of ADCs is calculated according to the data in [37]. Advanced CMOS technology will significantly reduce the power consumption of ADC.

TABLE II
POWER CONSUMPTION ANALYSIS.

condition	Pixel Power (uW)	Readout Power (uW)	ADC Power (uW)	Total Power (uW)	Efficiency (TOPS/W)	FoM (pJ/pixel/frame)
60FPS, 3×3, s=2	63.94	4.02	177.17	245.13	4.62	3.90
120FPS, 3×3, s=2	127.87	8.03	354.33	490.25	4.62	3.90
60FPS, 5×5 (splicing), s=2	177.60	4.02	177.17	358.79	8.77	5.70
60FPS, 5×5 (splicing), s=4	44.40	1.01	44.29	89.70	8.77	1.43
60FPS, 7×7 (splicing), s=2	348.10	4.02	177.17	529.29	11.65	8.41
60FPS, 7×7 (splicing), s=4	87.02	1.01	44.29	132.32	11.65	2.10

TABLE III
PERFORMANCE COMPARISON

	2017ISSCC [14]	2019ASSCC [24]	2020TCASii [22]	2020TCASi [23]	2021ISSCC [25]	this work
Process	90 nm/60 nm	180 nm	180 nm	180 nm	65nm	180 nm
Supply	3.3/2.9/1.8/1 V	0.5 V	1.8 V	2 V	0.8 - 1.2 V	1.8 V
Array Size	1296×976	128×128	32×32	32×32	160×128	128×128
Pixel Size (um²)	3.5×3.5	7.6×7.6	110×110	40×40	9×9	30×30
Frame Rate	1000 fps	480 fps	1000 fps	100 fps	96 - 1072 fps	3840 fps
data/weight width	4 bit/NA	8 bit/4 bit	1 bit/1 bit	1 bit/1 bit	8 bit/1.5 bit	8 bit/8 bit
Feature	Spatial-Temporal processing	1st-layer CNN, ED, Blur, Sharpen	1st-layer BNN	1st-layer BNN	2 - 64 conv, ROI	1st-layer CNN
Processing	Digital	Analog	Analog	Analog	Analog	Analog
Memory	Yes(Digital)	No	No	Yes(Analog)	No	No
Pixel complexity	3T	4T	88T, 32 caps	3T	40T, 1 cap	2.5T
Method	3D-stacked	switching-current-and-integration	dedicated SRAM	Kernel-Readout	pulse modulation	pulse modulation
Power	363 mW	91 uW	12.16 uW	1.8 mW	42 - 206 uW	89.7 - 529.29 uW
Efficiency (TOPS/W))	0.77	1.51	2.64	1.09	0.15-3.64	4.62 - 11.65
FoM (pJ/pixel/fr)	286.98	11.65	11.88	NA	2.5-103.9	1.43 - 8.41

Table II shows that the power consumption of our proposed sensor circuit is determined by the frame rate and the convolution kernel size. When the convolution kernel size keeps constant, the power consumption increases with the frame rate. With the same frame rate, the larger convolution kernel size leads to higher power consumption.

Computational efficiency (TOPS/W) changes remarkably in different conditions. The power consumption mainly comes from three parts: the convolution operation, the readout circuit, and the column ADCs. Though the number of convolution operations and the number of readouts vary in the same

proportion, the cost of ADCs remains unchanged, leading to increased computational efficiency when the amount of computation increases. For example, the efficiency is 4.62 TOPS/W and the frame rate is 60 fps when the kernel size is 3×3 and the stride is 2. It is increased to 11.65 TOPS/W when the kernel size is 7×7.

FoM (pJ/pixel/frame) increases with the amount of computation but decreases with frame rate because of the same reason as the computational efficiency. It mainly represents the influence of convolution kernel size on power consumption. The increase in convolution kernel size will lead to a rise in

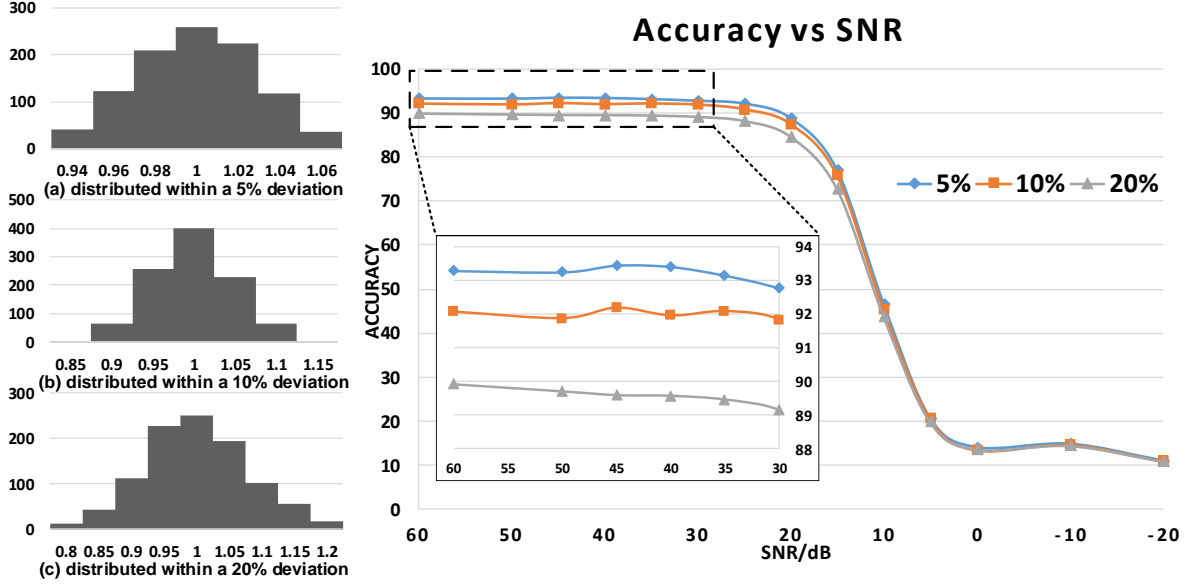


Fig. 16. Relationship between CNN accuracy and three types of disturbance.

the amount of computation and power consumption.

The change of stride will lead to different amount of computation. If the stride is doubled, the amount of computation and readout times will be reduced to a quarter, which leads to a decrease in power consumption and FoM.

As shown in Table III, the computing efficiency of our proposed architecture is up to 11.65 TOPS/W, which is three times as high as the latest in-sensor computing schemes. Since our proposed architecture integrates MAC operation with the pixel exposure, no additional analog computing circuit is used, leading to this high efficiency. The energy consumption of a single frame of figure has been estimated when a 7×7 kernel is adopted and stride is 2. A traditional CIS + DLA vision system consumes about 133.74 μ J (based on [9], [38]) and the proposed scheme costs only 8.82 μ J, which shows a 15 times reduction of the energy consumption. The energy consumption of the CIS is estimated based on the scaling of resolution and frame rate, and the energy consumption of the DLA is estimated by the product of the computational efficiency of the DLA and the computing amount.

C. Noise Analysis

Operations in the analog domain are affected by undesirable factors such as noise and variations. In this section, we analyze the robustness of our proposed circuits.

The temporal noise and Fixed Pattern Noise (FPN) are the most fundamental nonideality in CIS [26]. The sample noise at the end of integration can be expressed as the sum of: (1) integrated shot noise Q_{shot} , (2) reset noise Q_{reset} , (3) readout circuit noise Q_{read} due to readout device thermal and flicker (or $1/f$) noise, (4) offset FPN due to device mismatches Q_{FPN} , (5) offset FPN due to dark current variation, commonly referred to as dark signal nonuniformity (DSNU), and (6) gain

FPN, commonly referred to as PRNU. For a conventional CIS with a CDS operation, the total noise can be estimated by

$$S_2 - S_1 = Q_{shot} - Q_{1,read} + Q_{2,read} + Q_{DSNU} + Q_{PRNU} \quad (8)$$

in which the reset noise and the offset FPN are suppressed but the read noise power is increased.

In our proposed scheme, the CIS performs two exposures and readouts for positive and negative weights, respectively. After the subtract operation by the digital circuits, the noise can be estimated by

$$S_p - S_n = (Q_{p,shot} - Q_{n,shot}) + (Q_{p,reset} - Q_{n,reset}) + (Q_{p,read} - Q_{n,read}) + (Q_{p,PRNU} - Q_{n,PRNU}) \quad (9)$$

in which the offset FPN are suppressed, and most of low frequency noise will be reduced due to the short time interval between two readout (less than 32 μ s, about 30 KHz). Therefore, the proposed CIS does not add additional noise. In addition, the MAC operation on the pixel array may benefit the SNR, in the case of a 3×3 kernel this can be explained as

$$noise = E[(\frac{\sum n_{all}}{9})^2] = \frac{1}{9^2} D(\sum n_{all}) = \frac{\sigma^2}{9} \quad (10)$$

$$SNR = \frac{power}{noise} = 9 \frac{power}{\sigma^2} \quad (11)$$

in which n_{all} represents the total noise.

D. Algorithm Robustness

Through network simulation with Cifar-10 [39] dataset and Resnet-18, the accuracy of CNN changes with SNR or mismatch as shown in Fig. 16. As the proposed CIS only supports 1st-layer CNN, the rest of the computation is

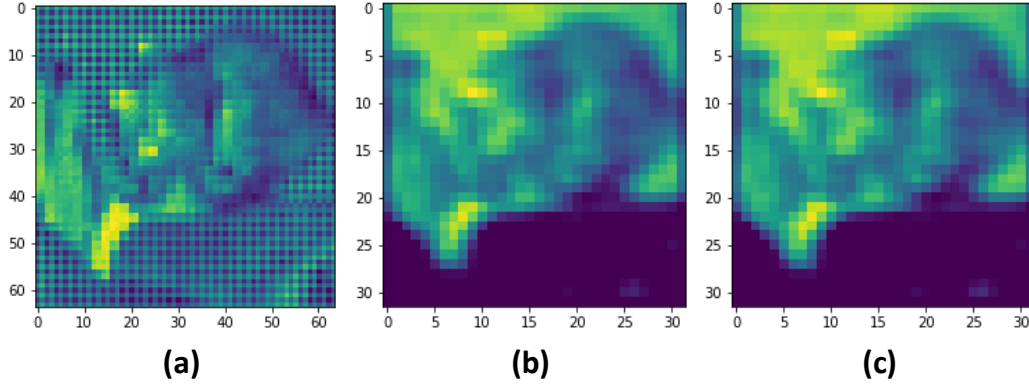


Fig. 17. (a) An input test figure (with RRGB pattern). (b) A channel of the output feature map of the 1-st layer CNN performed by the proposed CIS and (c) by CPU.

TABLE IV
MEAN RMS ERROR FOR THE 1-ST LAYER OUTPUT IN DIFFERENT CONDITION

SNR	60dB	40dB	20dB	0dB
5% deviation	6.78e-3	7.12e-3	2.25e-2	1.77e-1
10% deviation	1.13e-2	1.15e-2	2.43e-2	1.77e-1
20% deviation	1.80e-2	1.82e-2	2.80e-2	1.78e-1

performed externally. Three normal distributions with different variances of the equivalent capacitors are used to simulate the mismatch, and the distributions are shown in Fig. 16. The results only have a negligible accuracy loss when SNR is more than 40 dB. The typical SNR value for CIS is 40 dB - 60 dB [22]. Fig. 17 shows a comparison of the input RRGB figure and the output feature map of the 1-st layer CNN performed by CPU or the proposed CIS. The mean RMS error for the 1-st layer output of the proposed CIS is shown in Table. IV. As expected with the reduction in the SNR, the RMS error increases.

Because the first layer of CNN is sensitive to pruning and quantization, the conventional network model compression algorithms often leave the first layer untouched. For example, most layers may perform a 4-bit quantization, but the 1-st layer needs at least 8-bit to keep accuracy. In this case, DLAs must support 8-bit computing to support the entire net, which leads to extra costs and reduction of system efficiency. Moreover, due to the small number of input channels, DLAs' PEs are often not fully utilized for the first layer. Therefore, this design can improve the computational efficiency of the subsequent DLAs, leading to higher performance of the entire machine vision system.

E. Performance under Other Resolutions

In this subsection, we discuss the power consumption, frame rate, and Efficiency of the architecture under different resolutions to show the scalability.

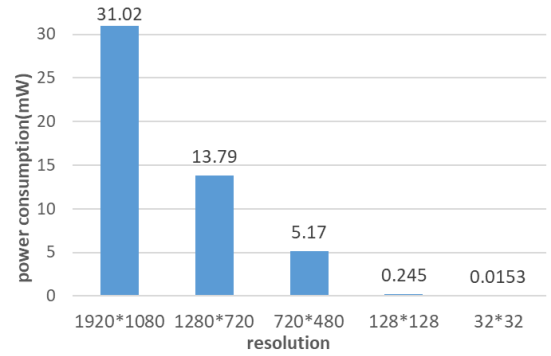


Fig. 18. The power consumption under different resolution. The illumination is about 1500 lux.

TABLE V
RATE CALCULATION UNDER DIFFERENT RESOLUTIONS.

resolution	minimum ADC frequency
1920×1080	2.76 MHz
1280×720	1.84 MHz
720×480	1.23 MHz
128×128	327.68 KHz
32×32	81.92 KHz

1) *Power Consumption*: Fig. 18 shows the power consumption of the proposed architecture under different resolutions. The power consumption is basically proportional to the amount of calculation thus increases with the resolution. Thus, the computation efficiency is independent of the resolution.

2) *Maximum Frame Rate*: According to Eq. 6, the maximum frame rate limited by exposure time is independent of resolution. As shown in Eq. 5, the minimum ADC frequency is proportional to the height of the array. The minimum ADC frequency under other resolutions is tabulated in Table V. The operation condition is all set to 3×3 kernel and stride is 2.

V. CONCLUSION

In this work, a PIP architecture has been proposed to perform the first layer convolution operation of CNN. It supports a variety of different convolution kernel sizes and parameters. The simulation results have shown that our proposed scheme functions correctly with good linearity. When the convolution kernel is 7×7 , the step size is 2, and the channel number is 64 at 60 fps, the proposed architecture consumes 529.29 μ W power and has a computational efficiency up to 11.65 TOPS/W. It is suitable for application scenarios with tight requirements on power consumption, such as daily monitoring and Internet of Things (IoT) devices.

REFERENCES

- [1] X. Chen, H. Li, Q. Wu, K. N. Ngan, and L. Xu, "High-Quality R-CNN Object Detection Using Multi-Path Detection Calibration Network," *IEEE Transactions on Circuits and Systems for Video Technology*, vol. 31, no. 2, pp. 715–727, 2021.
- [2] C. Ding and D. Tao, "Trunk-Branch Ensemble Convolutional Neural Networks for Video-Based Face Recognition," *IEEE Transactions on Pattern Analysis and Machine Intelligence*, vol. 40, no. 4, pp. 1002–1014, 2018.
- [3] L. Wu, K. Huang, H. Shen, and L. Gao, "Foreground-background Parallel Compression with Residual Encoding for Surveillance Video," *IEEE Transactions on Circuits and Systems for Video Technology*, pp. 1–1, 2020.
- [4] D. Wei, X. Xu, H. Shen, and K. Huang, "GAC-GAN: A General Method for Appearance-Controllable Human Video Motion Transfer," *IEEE Transactions on Multimedia*, pp. 1–1, 2020.
- [5] F. Zhou and Y. Chai, "Near-sensor and in-sensor computing," *Nature Electronics*, vol. 3, pp. 664–671, 2020.
- [6] M. T. Chung, C. L. Lee, C. Yin, and C. C. Hsieh, "A 0.5 V PWM CMOS Imager With 82 dB Dynamic Range and 0.055% Fixed-Pattern-Noise," *IEEE Journal of Solid-State Circuits*, vol. 48, no. 10, pp. 2522–2530, 2013.
- [7] A. Kaur, D. Mishra, K. M. Amogh, and M. Sarkar, "On-Array Compressive Acquisition in CMOS Image Sensors Using Accumulated Spatial Gradients," *IEEE Transactions on Circuits and Systems for Video Technology*, vol. 31, no. 2, pp. 523–532, 2021.
- [8] O. Kumagai, A. Niwa, K. Hanzawa, H. Kato, and Y. Nitta, "A 1/4-inch 3.9Mpixel low-power event-driven back-illuminated stacked CMOS image sensor," in *2018 IEEE International Solid - State Circuits Conference - (ISSCC)*, 2018.
- [9] A. Y. Chiou and C. Hsieh, "An ULV PWM CMOS Imager With Adaptive-Multiple-Sampling Linear Response, HDR Imaging, and Energy Harvesting," *IEEE Journal of Solid-State Circuits*, vol. 54, no. 1, pp. 298–306, 2019.
- [10] J. Choi, J. Shin, D. Kang, and D. Park, "Always-On CMOS Image Sensor for Mobile and Wearable Devices," *IEEE Journal of Solid-State Circuits*, vol. 51, no. 1, pp. 130–140, 2016.
- [11] A. Y. Chiou and C. Hsieh, "A 137 dB Dynamic Range and 0.32 V Self-Powered CMOS Imager With Energy Harvesting Pixels," *IEEE Journal of Solid-State Circuits*, vol. 51, no. 11, pp. 2769–2776, 2016.
- [12] B. Zhao, X. Zhang, S. Chen, K.-S. Low, and H. Zhuang, "A 64×64 CMOS Image Sensor With On-Chip Moving Object Detection and Localization," *IEEE Transactions on Circuits and Systems for Video Technology*, vol. 22, no. 4, pp. 581–588, 2012.
- [13] H. Zhu and T. Shibata, "A Real-Time Motion-Feature-Extraction VLSI Employing Digital-Pixel-Sensor-Based Parallel Architecture," *IEEE Transactions on Circuits and Systems for Video Technology*, vol. 24, no. 10, pp. 1787–1799, 2014.
- [14] T. Yamazaki, H. Katayama, S. Uehara, A. Nose, M. Kobayashi, S. Shida, M. Odahara, K. Takamiya, Y. Hisamatsu, S. Matsumoto, L. Miyashita, Y. Watanabe, T. Izawa, J. Muramatsu, and M. Ishikawa, "4.9 A 1ms high-speed vision chip with 3D-stacked 140GOPS column-parallel PEs for spatio-temporal image processing," in *2017 IEEE International Solid-State Circuits Conference (ISSCC)*, 2017, pp. 82–83.
- [15] M. F. Amir, D. Kim, J. Kung, D. Lie, S. Yalamanchili, and S. Mukhopadhyay, "NeuroSensor: A 3D image sensor with integrated neural accelerator," in *2016 IEEE SOI-3D-Subthreshold Microelectronics Technology Unified Conference (S3S)*, 2016, pp. 1–2.
- [16] Z. Du, R. Fasthuber, T. Chen, P. Ienne, L. Li, T. Luo, X. Feng, Y. Chen, and O. Temam, "ShiDianNao: Shifting vision processing closer to the sensor," in *2015 ACM/IEEE 42nd Annual International Symposium on Computer Architecture (ISCA)*, 2015, pp. 92–104.
- [17] Yunhui, Hou, Robert, LiKamWa, Lin, Zhong, Mia, Polansky, Julian, and Gao, "RedEye: Analog convNet Image Sensor Architecture for Continuous Mobile Vision," *Computer Architecture News*, 2016.
- [18] L. Bose, J. Chen, S. J. Carey, P. Dudek, and W. Mayol-Cuevas, "Fully Embedding Fast Convolutional Networks on Pixel Processor Arrays," 2020.
- [19] T. Hsu, Y. Chiu, W. Wei, Y. Lo, C. Lo, R. Liu, K. Tang, M. Chang, and C. Hsieh, "AI Edge Devices Using Computing-In-Memory and Processing-In-Sensor: From System to Device," in *2019 IEEE International Electron Devices Meeting (IEDM)*, 2019, pp. 22.5.1–22.5.4.
- [20] S. Han, H. Mao, and W. J. Dally, "Deep Compression: Compressing Deep Neural Network with Pruning, Trained Quantization and Huffman Coding," in *4th International Conference on Learning Representations (ICLR)*, 2016.
- [21] M. Rastegari, V. Ordonez, J. Redmon, and A. Farhadi, "XNOR-Net: ImageNet Classification Using Binary Convolutional Neural Networks," in *European Conference on Computer Vision (ECCV)*, 2016, pp. 525–542.
- [22] H. Xu, Z. Li, N. Lin, Q. Wei, F. Qiao, X. Yin, and H. Yang, "MACSen: A Processing-In-Sensor Architecture Integrating MAC Operations into Image Sensor for Ultra-Low-Power BNN-Based Intelligent Visual Perception," *IEEE Transactions on Circuits and Systems II: Express Briefs*, vol. 68, no. 2, pp. 627–631, 2021.
- [23] Z. Chen, H. Zhu, E. Ren, Z. Liu, K. Jia, L. Luo, X. Zhang, Q. Wei, F. Qiao, X. Liu, and H. Yang, "Processing Near Sensor Architecture in Mixed-Signal Domain With CMOS Image Sensor of Convolutional-Kernel-Readout Method," *IEEE Transactions on Circuits and Systems I: Regular Papers*, vol. 67, no. 2, pp. 389–400, 2020.
- [24] T. Hsu, Y. Chen, T. Wen, W. Wei, Y. Chen, F. Chang, H. Kim, Q. Chen, B. Kim, R. Liu, C. Lo, K. Tang, M. Chang, and C. Hsieh, "A 0.5V Real-Time Computational CMOS Image Sensor with Programmable Kernel for Always-On Feature Extraction," in *2019 IEEE Asian Solid-State Circuits Conference (A-SSCC)*, 2019, pp. 33–34.
- [25] M. Lefebvre, L. Moreau, R. Dekimpe, and D. Bol, "7.7 A 0.2-to-3.6TOPS/W Programmable Convolutional Imager SoC with In-Sensor Current-Domain Ternary-Weighted MAC Operations for Feature Extraction and Region-of-Interest Detection," in *2021 IEEE International Solid-State Circuits Conference (ISSCC)*, vol. 64, 2021, pp. 118–120.
- [26] A. El Gamal and H. Eltoukhy, "CMOS image sensors," *IEEE Circuits and Devices Magazine*, vol. 21, no. 3, pp. 6–20, 2005.
- [27] R. Eki, S. Yamada, H. Ozawa, H. Kai, K. Okuike, H. Gowtham, H. Nakanishi, E. Almog, Y. Livne, G. Yuval, E. Zyss, and T. Izawa, "9.6 A 1/2.3inch 12.3Mpixel with On-Chip 4.97TOPS/W CNN Processor Back-Illuminated Stacked CMOS Image Sensor," in *2021 IEEE International Solid-State Circuits Conference (ISSCC)*, vol. 64, 2021, pp. 154–156.
- [28] V. T. Lee, A. Alaghi, J. P. Hayes, V. Sathe, and L. Ceze, "Energy-efficient hybrid stochastic-binary neural networks for near-sensor computing," in *Design, Automation Test in Europe Conference Exhibition (DATE)*, 2017, pp. 13–18.
- [29] T. Ma, K. Jia, X. Zhu, F. Qiao, Q. Wei, H. Zhao, X. Liu, and H. Yang, "An Analog-Memoryless Near Sensor Computing Architecture for Always-On Intelligent Perception Applications," in *2019 IEEE International Conference on Integrated Circuits, Technologies and Applications (ICTA)*, 2019, pp. 150–155.
- [30] L. Mennel, J. Symonowicz, S. Wächter, D. K. Polyushkin, and T. Mueller, "Ultrafast machine vision with 2D material neural network image sensors," *Nature*, vol. 579, no. 7797, pp. 62–66, 2020.
- [31] K. Bong, S. Choi, C. Kim, D. Han, and H. Yoo, "A Low-Power Convolutional Neural Network Face Recognition Processor and a CIS Integrated With Always-on Face Detector," *IEEE Journal of Solid-State Circuits*, vol. 53, no. 1, pp. 115–123, 2018.
- [32] S. Wang, C.-Y. Wang, P. Wang, C. Wang, Z.-A. Li, C. Pan, Y. Dai, A. Gao, C. Liu, J. Liu, H. Yang, X. Liu, B. Cheng, K. Chen, Z. Wang, K. Watanabe, T. Taniguchi, S.-J. Liang, and F. Miao, "Networking retinomorphic sensor with memristive crossbar for brain-inspired visual perception," *National Science Review*, 07 2020, nwaal72.
- [33] H. Zimmermann, *Silicon optoelectronic integrated circuits*, 2nd ed. Cham, Switzerland: Springer, 2018;2019, vol. 13.
- [34] J. Gu, Y. Hitomi, T. Mitsunaga, and S. Nayar, "Coded rolling shutter photography: Flexible space-time sampling," in *2010 IEEE International Conference on Computational Photography (ICCP)*, 2010, pp. 1–8.

- [35] R. J. Perry and K. Arora, "Using PSPICE to simulate the photoresponse of ideal CMOS integrated circuit photodiodes," in *Proceedings of SOUTHEASTCON '96*, 1996, pp. 374–380.
- [36] A. Le Roch, C. Virmondois, P. Paillet, J.-M. Belloir, S. Rizzolo, F. Pace, C. Durnez, P. Magnan, and V. Goiffon, "Radiation-Induced Leakage Current and Electric Field Enhancement in CMOS Image Sensor Sense Node Floating Diffusions," *IEEE Transactions on Nuclear Science*, vol. 66, no. 3, pp. 616–624, 2019.
- [37] C.-C. Liu, S.-J. Chang, G.-Y. Huang, Y.-Z. Lin, and C.-M. Huang, "A 1V 11fJ/conversion-step 10bit 10MS/s asynchronous SAR ADC in 0.18 μ m CMOS," in *2010 Symposium on VLSI Circuits*, 2010, pp. 241–242.
- [38] Y. Li, X. Ding, H. Yang, X. Zhang, Y. Gong, and B. Liu, "A 681 GOPS/W 3.59 TOPS/W CNN Accelerator Based on Novel Data Flow Scheduling Scheme," in *2020 IEEE 15th International Conference on Solid-State Integrated Circuit Technology (ICSICT)*, 2020, pp. 1–3.
- [39] A. Krizhevsky and G. Hinton, "Learning multiple layers of features from tiny images," *Handbook of Systemic Autoimmune Diseases*, vol. 1, no. 4, 2009.

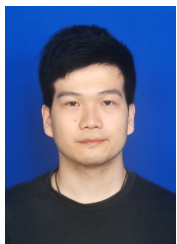


Ruibing Song (Student Member, IEEE) received a bachelor's degree from the College of Electrical Engineering, Zhejiang University, in 2020. He is currently pursuing a master's degree at the College of Information Science & Electronic Engineering, Zhejiang University. He is interested in in-sensor computing and in-memory computing.



Kejie Huang (Senior Member, IEEE) received the Ph.D. degree from the Department of Electrical Engineering, National University of Singapore (NUS), Singapore, in 2014. He has been a Principal Investigator with the College of Information Science Electronic Engineering, Zhejiang University (ZJU), since 2016. Before joining ZJU, he has spent five years in the IC design industry, including Samsung and Xilinx, two years in the Data Storage Institute, Agency for Science Technology and Research (A*STAR), and another three years in Singapore

University of Technology and Design (SUTD), Singapore. He has authored or coauthored more than 40 scientific articles in international peer-reviewed journals and conference proceedings. He holds four granted international patents, and another eight pending ones. His research interests include low power circuits and systems design using emerging non-volatile memories, architecture and circuit optimization for reconfigurable computing systems and neuromorphic systems, machine learning, and deep learning chip design. He currently serves as the Associate Editor of the IEEE TRANSACTIONS ON CIRCUITS AND SYSTEMS-PART II: EXPRESS BRIEFS.



Zongsheng Wang (Student Member, IEEE) received a bachelor's degree from the College of Electrical Engineering, Zhejiang University, in 2020. He is currently pursuing a master's degree at the College of Information Science & Electronic Engineering, Zhejiang University. He is interested in in-sensor computing, low power digital circuit design and deep learning accelerator.



Haibin Shen is currently a Professor with Zhejiang University, a member of the second level of 151 talents project of Zhejiang Province, and a member of the Key Team of Zhejiang Science and Technology Innovation. His research interests include learning algorithm, processor architecture, and modeling. His research achievement has been used by many authority organizations. He has published more than 100 papers in academic journals, and he has been granted more than 30 patents of invention. He was a recipient of the First Prize of Electronic Information Science and Technology Award from the Chinese Institute of Electronics, and has won a second prize at the provincial level.